ORIGINAL PAPER

Check for updates

Characterization and Assessment of Natural Amazonian Clays for Cosmetics-Industry Applications

Antonio Claudio Kieling · Cláudia Cândida Silva · Sérgio Duvoisin Júnior · José Costa de Macedo Neto · Miécio de Oliveira Melquíades · Gilberto Garcia del Pino · Yago Ono de Souza Moreira · Túlio Hallak Panzera · Maria das Graças da Silva Valenzuela · Francisco Rolando Valenzuela Diáz

Abstract Clays are abundant materials in the Amazon region and have been used historically by ancient Amazonian people to produce ceramic and cosmetics products. The current study aimed to evaluate the potential of four clays from the metropolitan area of Manaus, each with a different color, for cosmetics applications. Two clays were collected in the Ponta Negra region (red and gray in color) in Manaus, one in Careiro (white), and one in Itacoatiara (black). After drying in an oven for 24 h at 105°C, the four clays were characterized by X-ray fluorescence (XRF), X-ray diffraction (XRD), infrared (IR) spectroscopy, thermogravimetry (TGA), differential thermal analysis (DTA), differential scanning calorimetry (DSC), scanning electron microscopy (SEM), particle-size analysis, and detection of microorganisms. The amounts of Al, Si, Cl, K, Ca, Ti, Cr, Fe, Zn, P, and S in all samples were below the limits for use in cosmetics. The main phases identified were kaolinite 1A, quartz, gibbsite, and the rare kaolinite 2M. Approximately 40 wt.% of each sample was in the < 20 µm particle-size range. Analyses by SEM revealed pseudo-hexagonal kaolinite structures with nano-islands and nanocrystallites. The low toxicity, mineralogic compositions, and particle-size findings suggest that Amazonian clays are promising for cosmetics applications.

Keywords Clays · Cosmetics · Kaolinite · Physicochemical characterization

Associate Editor: F. Javier Huertas

A. C. Kieling · G. G. del Pino
Department of Mechanical Engineering, Amazonas State University – UEA, Manaus, Brazil

A. C. Kieling · C. C. Silva · S. D. Júnior ·
J. C. de Macedo Neto · M. de Oliveira Melquíades ·
G. G. del Pino · Y. O. de Souza Moreira ·
T. H. Panzera (✉) · M. da Silva Valenzuela · F. R. V. Diáz
Department of Education, Federal Institute of Amazonas –
IFAM, Manaus, Brazil
e-mail: panzera@ufsj.edu.br

C. C. Silva · S. D. Júnior · Y. O. de Souza Moreira
Department of Chemical Engineering, Amazonas State University – UEA, Manaus, Brazil

J. C. de Macedo Neto
Department of Materials Engineering, Amazonas State University – UEA, Manaus, Brazil

M. de Oliveira Melquíades · T. H. Panzera
Department of Mechanical Engineering, Federal University of São João del Rei – UFSJ, São João del Rei, Brazil

M. da Silva Valenzuela · F. R. V. Diáz
Department of Metallurgical and Materials Engineering, University of São Paulo – USP, São Paulo, Brazil

Ⓐ Springer

Introduction

Clays are fine-grained, natural soil materials that possess a range of peculiar chemical, mineralogic, and granulometric properties, as well as some plasticity in terms of mechanical properties when mixed with an appropriate amount of water. The structure, the colloid size of the particles, and their constitution give rise to the desired rheological characteristics and sorption capacities. Clays often contain minerals such as quartz, feldspar, carbonates, sulfates, and iron, aluminum, and titanium oxides. These minerals can affect the chemical (e.g. stability and purity), physical (e.g. texture, moisture content, and particle size), and toxicological requirements specified for each clay application (Morekhure-Mphahlele et al., 2017). In this context, the characterization of clays is essential as the ideal combination of composition and structure can lead to optimal performance for the target application (Bouna et al., 2020).

The toxicological issue mentioned is linked directly to the application of clays in the pharmaceutical industry. The most common clays for pharmacological applications are kaolinite ($Al_2Si_2O_5$), talc, smectites, palygorskite, and sepiolite (Massaro et al., 2018). Kaolin ($Al_2H_4O_9Si_2$) with iron oxide was studied by Long et al. (2018) with a view to controlling bleeding and improving wound-healing performance. Those authors characterized its crystal structure, morphology, coagulation, adsorption, and toxicity by means of kaolin zeta potential, platelet aggregation, XRD, SEM, Fourier-transform infrared spectroscopy (FTIR), cytotoxicity, and hemolysis assays. Kaolinite is applied in gastrointestinal protectors, antidiarrheal products, dermatological protectors, local anesthetics, cosmetic creams, powders, anti-inflammatories, and emulsions (Carretero & Pozo, 2010).

Among the range of possibilities cited by the pharmaceutical industry, the potential application of clays as cosmetic products, i.e. in which the material is placed in contact with the outside of the human body, was the focus of the current work. The motivation was linked to the high demand for raw materials in the global cosmetics market; western Europe and North America have the largest share of the world market for cosmetics ingredients, valued at > €30 billion annually. Europe was the world's largest cosmetics market in 2019 when the price of cosmetics containing these ingredients reached €80 billion (Cosmetic Europe, 2019).

The present work focused on clay extracted from South America, especially kaolinite. Estimates of kaolinite production in the State of Amazonas, in the region of Manaus, Brazil, suggest a production of 500,000 tons/year of kaolin, with a useful production potential of $60 million and a life expectancy of 50 years (Reis et al., 2006). Official policy, however, allocates kaolin reserves to white ceramics, paint, and varnish manufacture, and to the electro-electronics industry (Reis et al., 2006). There is, therefore, a potential for trade in the cosmetics industry that has not yet been explored fully. Products composed of kaolinite are common in the global market: Aloe Vera and kaolinite have been combined to create peel-off mask gel compositions (Beringhs et al., 2013); the potential of emulsions made with kaolin and an ethanolic extract of the *Litchi chinensis* leaf to inhibit UVB-induced photodamage was investigated by Thiesen et al. (2020).

The literature on kaolinite in the Manaus region deals with mineralogic characterization and transformations (Chauvel et al., 1987; Cornu et al., 1999; Horbe et al., 2004). The kaolinitic mineralogy of Manaus comprises kaolinite with low isomorphic substitution by iron and mixture with quartz, gibbsite, and goethite. As expected, the kaolinite from Manaus has a clay-mineral structure (1:1 layer type) with low isomorphic substitution and low cation-exchange capacity (Silva et al., 2017). In addition, kaolin from the Manaus region is a poorly ordered clay mineral, retaining 2.21% of water (Couceiro & Santana, 1999) and having low cation adsorption (Souza & Santana, 2014). This set of properties seems suitable for pharmaceutical applications and has motivated this study to evaluate its potential for the cosmetics industry.

Here, the physical and chemical properties of four samples of clay minerals extracted from the State of Amazonas were studied. The new contributions compared to previous works are based on a broad characterization of clays from the largest biome in the world, carefully evaluating their properties from a pharmacological point of view.

Materials and Methods

Materials

The clays were collected at four locations in Amazonas, Brazil (Fig. 1), at 1–2 m of soil depth. The

Fig. 1 Locations and colors of the clay samples

geographical coordinates were identified on a GPS device (GPS Data-Smart):

- Ponta Negra clay 1 (red): collected at Manaus, Amazonas, in the Ponta Negra region (3°02′53.6″ S, 60°05′22.4″ W). Code: APN-1.
- Ponta Negra clay 2 (gray): collected at Manaus, Amazonas, in the Ponta Negra region (3°03′26.5″ S, 60°06′20.0″ W). Code: APN-2.
- Kaolin AM (white): collected at Careiro, Amazonas, (3°49′10.0″ S, 60°21′40.4″ W). Code: Kaolin.
- Black clay AM (black): collected at Itacoatiara, Amazonas, (3°08′58.9″ S, 58°6′13.5″ W). Code: AN-Am.

Sieve Analysis

Initially, the sample material was oven dried for 24 h at 105°C. Then the material was passed through a tower of sieves consisting of 11 screens with the following mesh sizes (in mm): (1) 2.00; (2) 1.41; (3) 1.00; (4) 0.59; (5) 0.42; (6) 0.35; (7) 0.25; (8) 0.18; (9) 0.125; (10) 0.075; (11) (pan). The set of sieves was vibrated for 2 h until the material passed through all the sieves and reached the bottom. Then the

amount retained on each sieve was weighed and the values were noted and tabulated for each sample. The standard for particle-size analysis was ASTM D6913/D6913M (2017).

Moisture Analysis

The humidity content was calculated by Eq. 1:

$$\text{Humidity} = \frac{(\text{wet weight} - \text{dry weight})}{\text{dry weight}} \times 100 \quad (1)$$

Approximately 16 g of each wet material was placed in an oven at 105°C for 24 h. Then the material was placed in a desiccator to cool. An analytical balance with a resolution of 0.0001 g (TW223L, Shimadzu, Tokyo, Japan) was used according to ASTM D2216 (2019) protocols.

X-ray Fluorescence Analysis

Three samples (1.5 g) of each material were packed in an Eppendorf tube, and each sample was run 18 times. Prior to WD-XRF testing, 0.4 g of boric acid was added and mixed with the sample material. Subsequently, tablets with uniform granulometry were

prepared by uniaxial pressing at 98 kPa. The mixture comprised 1000 g of the sample homogenized with 4000 g of high-purity H_3BO_3 in an agate mortar. All samples were analyzed in triplicate.

Analyses were performed using an XRF instrument (Rigaku, supermini model, Wilmington, Delaware, USA) using wave dispersion (WD-XRF) and a palladium tube, with an exposure time of 200 s at a power of 200 W. All elements were identified by their Kα and/or Kß energies (Ma & Allen, 2004). Equipment calibrations were carried out using LIF 200, PET, and RX25 crystals with scintillation (SC) and proportional (PC) counter detectors. Geological reference standards such as GBW 3125, 7105, and 7113 were also used for equipment calibration.

Each element was quantified using patterns of external salts of known purity diluted in boric acid. Quantifications were performed based on their intensities (cps/uA) using the ZSX-spectrometer *Status* program (Rigaku Corporation, 2008), considering the recommendations of the ASTM E1621 (2013) and ASTM C114 (2013) standards. At least six predetermined concentrations submitted to the same analysis conditions were considered.

X-ray Diffraction Analysis

Kaolin samples Ponta Negra clay 1 (APN-1), Ponta Negra clay 2 (APN-2), Black clay AM (AN-Am), and Kaolin AM were evaluated. The clays were ground in an agate mortar before pressing in the sample holder. A diffractometer (Empyrean, Malvern Panalytical, Malvern, UK) with CuKα radiation ($\lambda = 0.1541838$ nm), and an angular range of 5–85°2θ, with acceleration voltage and current of 40 kV and 40 mA, respectively, was used. The step size and the time per step were 0.02°2θ and 2 s, respectively. The X-ray photons were detected by an area detector (PIXcel3D-Medipix3 1×1).

The diffractograms obtained were indexed against the patterns of the Inorganic Crystal Structure Database – ICSD. All patterns were submitted to the Rietveld method and the *GSAS-EXPGUI* program package (Larson & Von Dreele, 2004) to refine the structural parameters and, thus, obtain the crystalline cell for the synthesized phase, lattice parameters, crystallite size, and micro tension, and to quantify the current phases. An 8th-order Chebyshev polynomial was chosen. The pseudo-Voigt function convoluted

with an asymmetric function of Finger, Cox, and Jephcoat was used to adjust the profile (Larson & Von Dreele, 2004), based on Stephens' phenomenological model, which considers anisotropic line broadening from microstrains (Paiva-Santos, 2001). The Crystallographic Information File (CIF), corresponding to the identified phases, was used to refine the sample. Due to the instrumental contribution, broadening corrections were made by refining a pattern of lanthanum hexaboride (LaB_6) obtained under the same sample conditions.

The broadening of the peaks was analyzed by the single-line method to calculate the crystallite size and lattice microtension (Ferreira et al., 2015; Michielon De Souza et al., 2016; Yadav et al., 2005). The average size of the crystallites was calculated using the Scherrer formula (Muniz et al., 2016), as follows:

$$D = 0.91\lambda/(\beta\_L \cos\theta) \tag{2}$$

and the microtension was estimated by the Stokes and Wilson (1944) equation as follows:

$$\varepsilon = \beta\_G/(4 \tan\theta) \tag{3}$$

In these Eqs. (2 and 3), λ is the wavelength used in diffraction measurements, and θ is the Bragg angle, while ß_L and ß_G are the Lorentzian and Gaussian contributions, respectively. Through the pseudo-Voigt function they can be calculated using the maximum width up to half-height (Γ), and the mixture coefficient parameter (η) can be obtained directly from the analysis using the Rietveld method (Michielon De Souza et al., 2016), as follows:

$$\beta\_G = \Gamma/2[\pi(1 - 0.74417\eta - 0.24781\eta^2 - 0.00810\eta^3)/\ln2]^{(1/2)} \tag{4}$$

$$\beta\_L = \pi\Gamma/2(0.72928\eta + 0.19289\eta^2 + 0.07783\eta^3) \tag{5}$$

All samples were submitted to a conventional X-ray diffractometer with a copper source (Cu), and the results were tabulated and transformed into a '.txt' format for analysis. *Origin*™ software was used along with the crystallinity analysis taken from XRD patterns. Three points were considered: baseline, number of peaks, and integration interval. The Adjacent-Averaging method performs normalization and smoothing of the data, considering five points. Data were scored from 0 to 100% to improve visualization and accuracy. The baseline was the

parameter for all calculations; thus, it was modeled to fit the peaks and obtain the areas of the crystalline peaks. The 'peak analysis' feature was used, and each peak was labeled. Then, the integration region was defined based on where each peak began and ended. Crystallinity was obtained by the percentage ratio between the area of crystalline peaks and the total area.

The presence of minerals was identified by visualizing the highest-intensity peaks with a mineral file obtained from the *American Mineralogist* Crystal Structure Database (http://rruff.geo.arizona.edu/AMS/amcsd.php). The main procedures were based on ASTM C1365 (2006) protocols.

Fourier-Transform Infrared Spectroscopy Analysis

Samples of 10–20 mg were characterized using an FTIR spectrophotometer (IRAffinity-1S, Shimadzu, Tokyo, Japan) according to ASTM E1252-98 (2021). The analysis was performed on the attenuated total reflectance (ATR) module (%T as a function of the wavenumber in cm^{-1}). The spectra were obtained in the MIR region from 4000 to 500 cm^{-1} and from 1550 to 1850 cm^{-1}.

Thermal Analysis

The TGA/DTA/DSC analysis was performed using a Mettler Toledo device (Columbus, Ohio, USA) from 30 to 1200°C with an increment of 10°C/min. N_2 at a flow rate of 50 mL/min was used according to ASTM E1131 (2020).

Scanning Electron Microscopy Analysis

Samples were prepared using a solution consisting of 10 mL of ethyl alcohol and 100 mg of material to be analyzed mixed in a 10 mL beaker. The solution was stirred until the clay was dispersed completely, and a homogeneous solution was formed. Subsequently, the solution was applied to the sample holders (stubs) using a graduated pipette. Samples were dried at room temperature. The sample was then sputter coated with Au alloy using a DII-29010SCTR (Jeol, Tokyo, Japan) instrument for 4 min. The microstructural analysis was conducted using a JSM-IT500HR microscope (Jeol), according to ASTM E986 (2004).

Particle-Size Distribution

After manual homogenization, the sample was mixed in 20 mL of distilled water (samples B, C, D, F). One drop was placed on the slide using a pipette and spread with a glass slide. Three drops of Tween 80 were used for complete dispersion for samples A, E, and H.

Optical microscopy analysis was performed to obtain two-field images of the sample at magnifications of 50, 100, 200, and 500× using dark field incident light mode. Samples dispersed in water were characterized at magnifications of 50, 100, and 200×. A laser diffraction particle-size analyzer (MAZ3000, Malvern Panalytical, Malvern, UK) was used with distilled water to disperse the particles, considering a refractive index of 1.56, absorption of 0.1, stirring and pumping at 1750 rpm. Samples C and D were kept for 3 and 1 min, respectively, in ultrasound (100%) before testing.

Mie's mathematical model was used, considering that the particles were not opaque and had a spherical shape. This model finds the diffraction and diffusion of light in the particle and the medium. The analysis was performed following ASTM D4464 (2015).

Microbiological Analysis

The microorganisms were detected by placing the samples in an autoclave for 3 h at a pressure of 120 kPa. Then, the samples were sent to a continuous air circulation oven for 24 h at 105°C. Subsequently, the sample containers were placed in an autoclave at a pressure of 150 kPa for 15 min. Then they were dried for 30 min using an ultraviolet chamber. The samples were packed into appropriate containers and placed in a desiccator. These procedures followed Brazilian Resolutions 481/99 (BRAZIL, 1999) and (PHARMACOPEIA, 2008) and Favero et al. (2019).

Results

Sieve Analysis

The sieve distribution of clays collected in Amazonas is shown in Table 1. Kaolin, AN-Am, APN-1, and APN-2 have mass fractions of <20% above the 200-mesh sieve (0.075 mm). The mass fraction that passed through the 0.420 mm sieve ranged from 68

Table 1 Particle-size distribution

Ø sieve (mm)	Kaolin (%)	APN-1 (%)	APN-2 (%)	AN-Am (%)
$2.000 \leq x$	0	2	3	4
$1.400 \leq x < 2.000$	0	4	3	7
$1.000 \leq x < 1.400$	1	4	6	7
$0.590 \leq x < 1.000$	2	13	7	14
$0.420 \leq x < 0.590$	6	22	32	16
$0.350 \leq x < 0.420$	6	10	5	4
$0.250 \leq x < 0.350$	9	12	13	12
$0.180 \leq x < 0.250$	30	11	9	9
$0.125 \leq x < 0.180$	20	6	6	9
$0.075 \leq x < 0.125$	9	6	4	4
$x < 0.075$	17	10	12	14

to 97%, which shows that the material collected from this region is composed of fine particles.

Commercial products are generally composed of a fine-grained powder (no more than 0.5% of particles were > 75 μm) and aggregates ranging from 50 to 300 μm; however, fine particles should be < 2 μm (López-Galindo et al., 2007).

Moisture Analysis

The moisture percentages in kaolin, APN-1, APN-2, and AN-Am clays are listed in Table 2. The moisture content of kaolin is substantially less (0.40%) than the others, possibly because its source is relatively well protected from the natural moisture of the soils. The AN-Am sample, collected in Itacoatiara city, has the greatest moisture content (38.6%), followed by APN-1 and APN-2, collected near the Negro River in Manaus.

X-ray Fluorescence Analysis

The data obtained using the X-ray fluorescence by wave dispersion (WD-XRF) technique are shown

Table 2 Moisture content in the investigated clays

Soil samples	Mass before oven drying (g)	Mass after oven drying (g)	Mass variation (g)	Moisture content (%)
Kaolin	16.94	16.88	0.06	0.4
APN-1	17.75	14.36	3.40	19.1
APN-2	16.80	14.87	1.93	11.5
AN-Am	16.61	10.20	6.41	38.6

in Table 3. Seventeen (17) different elements were observed, with emphasis on Al, Si, Cl, K, Ca, Ti, Cr, Fe, Zn, P, and S. The compositional, technical, and safety specifications of clays for use as pharmaceutical and cosmetic products show that the permissible limits for elements traditionally considered toxic (As, Sb, Cd, Co, Cu, Pb, Ni, Zn, Hg, Se, Te, TL, Ba, etc.), and other less dangerous elements (Li, Rb, Sr, Cr, Mo, V, Zr), must be strictly controlled, as reported by López-Galindo et al. (2007). All clays are within the permitted limits, except for Cr, for which the recommended limit of 50 ppm is met by the kaolin sample only.

Elements present at lower concentrations, such as Cu, Mg, Ni, Mn, and Sr, were observed in a few samples. Kaolin contains no Mg, Ni, Mn, or Sr. The AN-Am sample contains no Ni, Mn, or Sr, and APN-2 contains no Cu, Ni, Mn, or Sr. APN-1 does not contain Mn. This implies that these clays must possess unique properties that would be suitable for various cosmetics applications.

The presence of Al or Si was expected as all phases observed by XRD contain these elements. However, the Si/Al ratio for the three types of kaolinites is as follows: Kaolin < APN-1 ≈ APN-2 < AN-Am. All elements observed have already been reported, to a greater or lesser extent, as associated with the soils where the samples were obtained (Horbe et al., 2004).

X-ray Diffraction Analysis

The XRD results are shown in Fig. 2. The dominant phase in the clays belongs to the triclinic crystalline

Table 3 X-ray fluorescence analysis

Samples	Kaolin	APN-1	APN-2	AN-Am	LOD
Wt.% oxides					
Al_2O_3	54.92 ± 3.20	44.34 ± 2.10	42.56 ± 1.90	32.84 ± 1.80	0.002
SiO_2	43.43 ± 3.90	52.79 ± 2.20	51.37 ± 2.00	63.39 ± 2.51	0.002
	0.79	1.19	1.21	1.93	
Fe_2O_3	-	-	$3.00 \pm$	-	0.001
ppm					
Fe	2440 ± 115	6140 ± 180	-	2380 ± 127	12.0
Cl	160 ± 17	60 ± 15	60 ± 17	120 ± 21	2.0
K	280 ± 13	1750 ± 25	500 ± 22	3110 ± 28	4.8
Ca	180 ± 19	230 ± 21	310 ± 27	380 ± 23	2.2
Ti	1100 ± 95	4340 ± 105	3970 ± 112	2390 ± 109	2.5
Cr	50 ± 18	70 ± 17	80 ± 19	70 ± 21	2.2
Zn	40 ± 5	60 ± 6	10 ± 3	240 ± 9	1.2
Zr	180 ± 20	260 ± 22	440 ± 25	450 ± 27	2.0
P	20 ± 5	200 ± 18	170 ± 16	320 ± 21	1.2
S	90 ± 11	260 ± 13	230 ± 17	710 ± 23	1.6
Cu	20 ± 4	100 ± 9	0	50 ± 8	1.2
Mg	ND	890 ± 19	200 ± 21	260 ± 17	34.2
Ni	ND	30 ± 5	ND	ND	1.5
Mn	ND	ND	ND	ND	1.9
Sr	ND	10 ± 3	ND	ND	2.2
	99.57	99.89	98.74	99.16	

ND = Not detected, average ± std, in triplicate

The results were recalculated with respect to the loss on ignition (LOI) at 1000°C

system and $P1$ space group (No. 1), known as the 1A kaolinite mineral. Other than for CI and kaolin samples, it was also possible to identify the existence of a special clay, which is commercially rare, known as kaolinite 2M, which has a partial dickite-type structure with monoclinic symmetry and $C1c1$ space group (No. 9) (Vieira Coelho et al., 2007). A quartz phase, belonging to the trigonal crystalline system and space group $P3_121$ (No. 152), is present in the clays. A gibbsite phase was also identified in the APN-1 and kaolin samples. Gibbsite has a monoclinic crystalline system with a $P12_1/n$ (No. 14) space group 1.

All samples underwent refinement using the Rietveld method. Minimum residual and statistical parameters, χ^2 and R_{wp}, show proper adjustments (Fig. 3) (Toby, 2006). The deconvolution of the existing phases in the samples and their respective mass percentages are shown in Fig. 3. The network parameters of the unit cell of the phases were obtained after refinement and are listed in Table 4.

The mean value of crystallite size and microtension was calculated for the dominant phase of the samples, i.e. kaolinite 1A (Table 4). The phase has crystallite sizes with nanometric dimensions and microtension with values between 0.3 and 1.0%. Microtension is associated directly with the density of defects in the sample (Melquiádes et al., 2019; Soares de Oliveira et al., 2020). Materials with nanometric dimensions may have differentiated properties compared to bulk materials and be of interest for possible use in various technological applications (Das et al., 2015; Zhao et al., 2014). The values obtained for the crystallinity calculations of the evaluated materials are listed in Table 4. These results are similar to those of Couceiro and Santana (1999) and Silva et al. (2017).

X-ray diffraction shows the existence of practically homogeneous clays formed by clay minerals with low cation exchange capacity values, with results similar to those obtained by Souza and Santana (2014). In this way, these samples, when manipulated for the
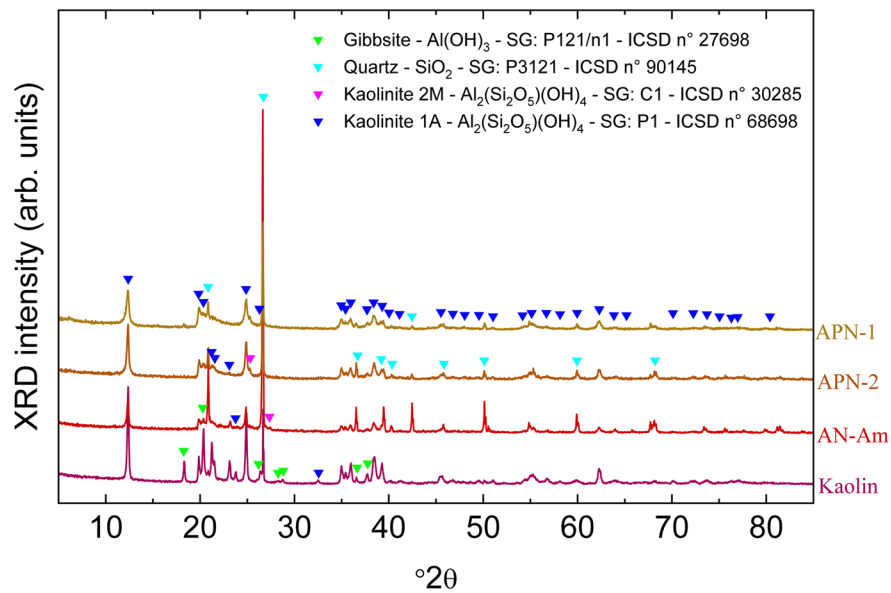
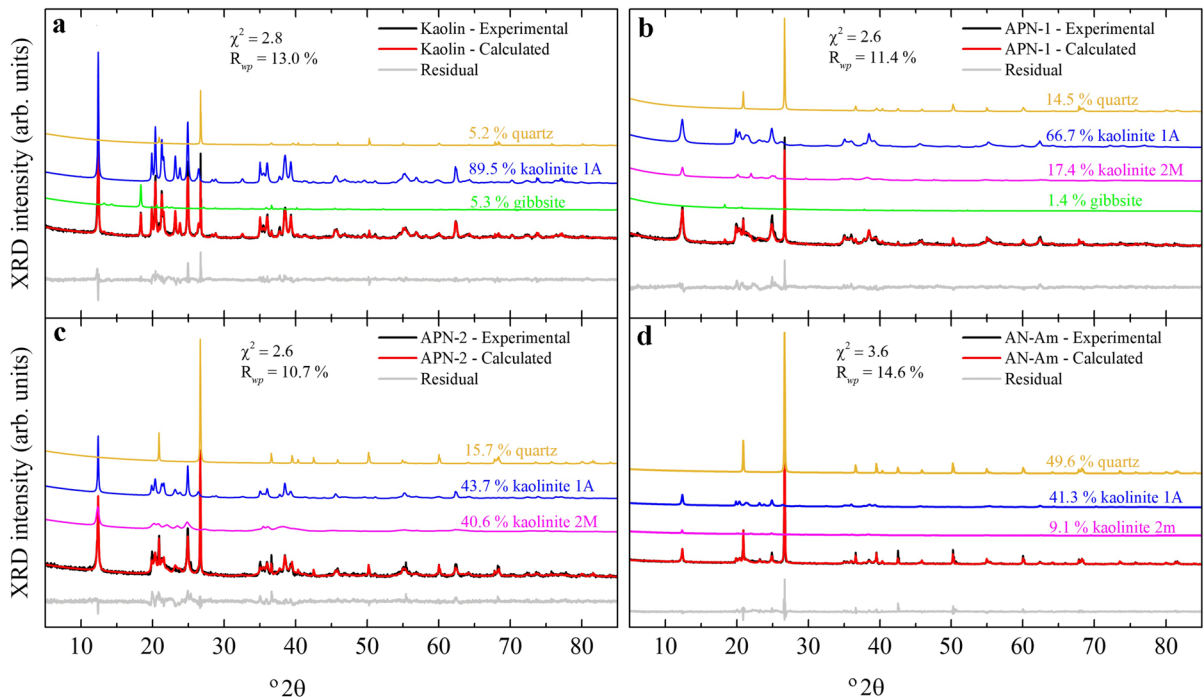**Fig. 2** Phase identification of kaolin, APN-1, APN-2, and AN-Am

Fig. 3 Refinement using the Rietveld method along with statistical parameters of refinement quality (χ^2 and R_{wp}) and phase deconvolution of samples **a** kaolin, **b** APN-1, **c** APN-2, and **d** AN-Am

Table 4 Parameters obtained after the Rietveld refinement method

Phases	Kaolin	APN-1	APN-2	AN-AM
Kaolinite 1A	$a = 0.5154(3)$	$a = 0.5160(1)$	$a = 0.5151(1)$	$a = 0.5156(2)$
	$b = 0.8938(6)$	$b = 0.8934(1)$	$b = 0.8932(2)$	$b = 0.8932(2)$
	$c = 0.7399(6)$	$c = 0.7391(2)$	$c = 0.7385(1)$	$c = 0.7399(2)$
	$D = 39.7(2)$	$D = 17.5(5)$	$D = 30.7(6)$	$D = 27.5(5)$
	$\varepsilon = 0.3(1)$	$\varepsilon = 0.6(1)$	$\varepsilon = 0.3(1)$	$\varepsilon = 0.4(1)$
	89.5%	66.7%	43.7%	49.3%
Kaolinite 2M		$a = 0.5151(5)$	$a = 0.5141(3)$	$a = 0.5160(1)$
		$b = 0.8950(1)$	$b = 0.8924(7)$	$b = 0.8910(2)$
		$c = 1.4520(2)$	$c = 1.457(1)$	$c = 1.4580(2)$
		17.4%	40.6%	9.1%
Quartz	$a = 0.4903(2)$	$a = 0.4908(4)$	$a = 0.4908(3)$	$a = 0.4909(2)$
	$b = 0.4903(2)$	$b = 0.4908(4)$	$b = 0.4908(3)$	$b = 0.4909(2)$
	$c = 0.5395(4)$	$c = 0.5398(1)$	$c = 0.5402(6)$	$c = 0.5402(2)$
	5.2%	14.5%	15.7%	49.6%
Gibbsite	$a = 0.8638(4)$	$a = 0.8590(1)$		
	$b = 0.5072(1)$	$b = 0.5060(1)$		
	$c = 0.9708(2)$	$c = 0.9709(6)$		
	5.3%	1.4%		
	Crystallinity (%)			
	76.548	80.192	78.439	83.164

$D = <D> (nm)$, $\varepsilon = <\varepsilon> (\%)$, and a, b, $c =$ lattice parameters

production of cosmetics and commercialization, offer a low risk of contamination (Mattioli et al., 2016).

Fourier-Transform Infrared Spectroscopy Analysis

For clarity, the combined spectra for the samples are shown in Fig. 4 and Table 5. The FTIR spectra of clay mineral samples revealed kaolinites with crystalline structure defects (Silva et al., 2017). The FTIR spectra generally show O–H stretch bands of medium to strong intensities between 3700 and 3300 cm^{-1}. Si–O stretching bands occurred between 1095 and 1009 cm^{-1} in the clay minerals, and Si–O–Si bands of quartz and Al–O fold were at 1200–700 cm^{-1}. SiO$_2$ had a strong band at ~1100 cm^{-1}, bending bands at 600–150 cm^{-1}, and medium SiO$_2$ bands at ~470 cm^{-1}. O–H metal bands were seen in folded mode between 950 and 600 cm^{-1}. Water absorbs below 800 cm^{-1}, and strong infrared transitions of metal-to-metal groups occurred at 800–200 cm^{-1} (Ihekweme et al., 2020).

Thermal Analysis

The results are shown for differential scanning calorimetry (DSC-Fig. 5a), thermogravimetric analysis (TGA-Fig. 5b) and differential thermal analysis (DTA-Fig. 5c) of kaolin, APN-1, PN-2) and AN-Am.

The thermal behavior of the various clay samples was quite similar. The first endothermic peak occurred near 100°C (DTA curve), where free water was lost between the particles. At ~220°C (DSC curve), the endothermic peak occurred due to the combustion of organic matter and water loss from the hydroxides attributed to the gibbsite.

The presence of hydroxides requires additional energy for their decomposition. The highest-intensity endothermic peak occurred at ~500°C, due to the loss of hydroxyl in the kaolinite group. Above 500°C, the crystallinity disappeared with the water loss and metakaolinite began to form; this is amorphous and metastable. The graph does not show the vitrification phase which should start at ~900°C with spinel formation; neither
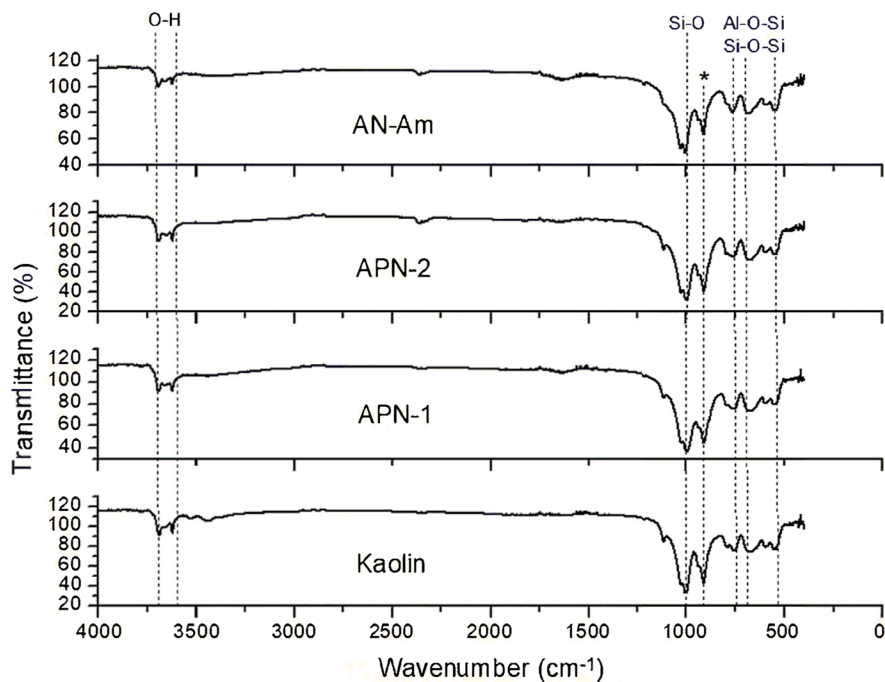
Fig. 4 FTIR spectra of samples kaolin, APN-1, APN-2, and AN-Am

Table 5 Frequencies and absorbance for various stretching and bending bands (cm^{-1})

Sample name	O–H Stretching	Si–O Stretching	Al–OH bending	Al–O–Si, Si–O–Si, Si–O Stretching
Kaolin AM (kaolin)	3,687–3,619	1,001–756	908	669–552
Ponta Negra Clay 1 (APN-1)	3,692–3,623	998–56	908	673–548
Black Clay AM (AN-Am)	3,691–3,622	1,002–760	907	682–544
Ponta Negra Clay 2 (APN-2)	3,688–3,619	998–759	908	597–548

does it show mullite nucleation, which should have begun at 970°C (Macedo et al., 2008).

The TGA analysis showed the loss of mass with increasing temperature. Note that the most significant mass loss was due to the dehydroxylation of kaolinite at ~500°C, and the total value of the mass loss was ~14% (kaolin sample), 13% (APN-1), 10% (APN-2), and 25% (AN-Am). These values are consistent for kaolin clays and corroborate the values found in the XRF analysis (e.g. Macedo et al., 2008).

Scanning Electron Microscopy Analysis

The microstructural analysis of kaolin (a–b), APN-1 (c–d), AN-Am (e–f), and APN-2 (g–h) (Fig. 6) revealed a hexagonal shape for kaolinite in the kaolin sample (Fig. 6a) and the presence of a nanocrystallite (Fig. 6b), similar to that reported by Lebedeva and Fogden (2011). The presence of pseudo-hexagonal lamellae in APN-1 (Fig. 6c–d) is a characteristic of kaolinite minerals (Otieno et al., 2019). Likewise, the AN-Am sample exhibited pseudo-hexagonal lamellae (Fig. 6e). The lamellae are slightly bent with a concave shape (Fig. 6f). This morphology is probably due to the loss of tension in the crystalline structure of the lamellae (Neto et al., 2017). The Ponta Negra (APN-2) sample also contained pseudo-hexagonal lamellae characteristic of kaolinite (Otieno et al., 2019).

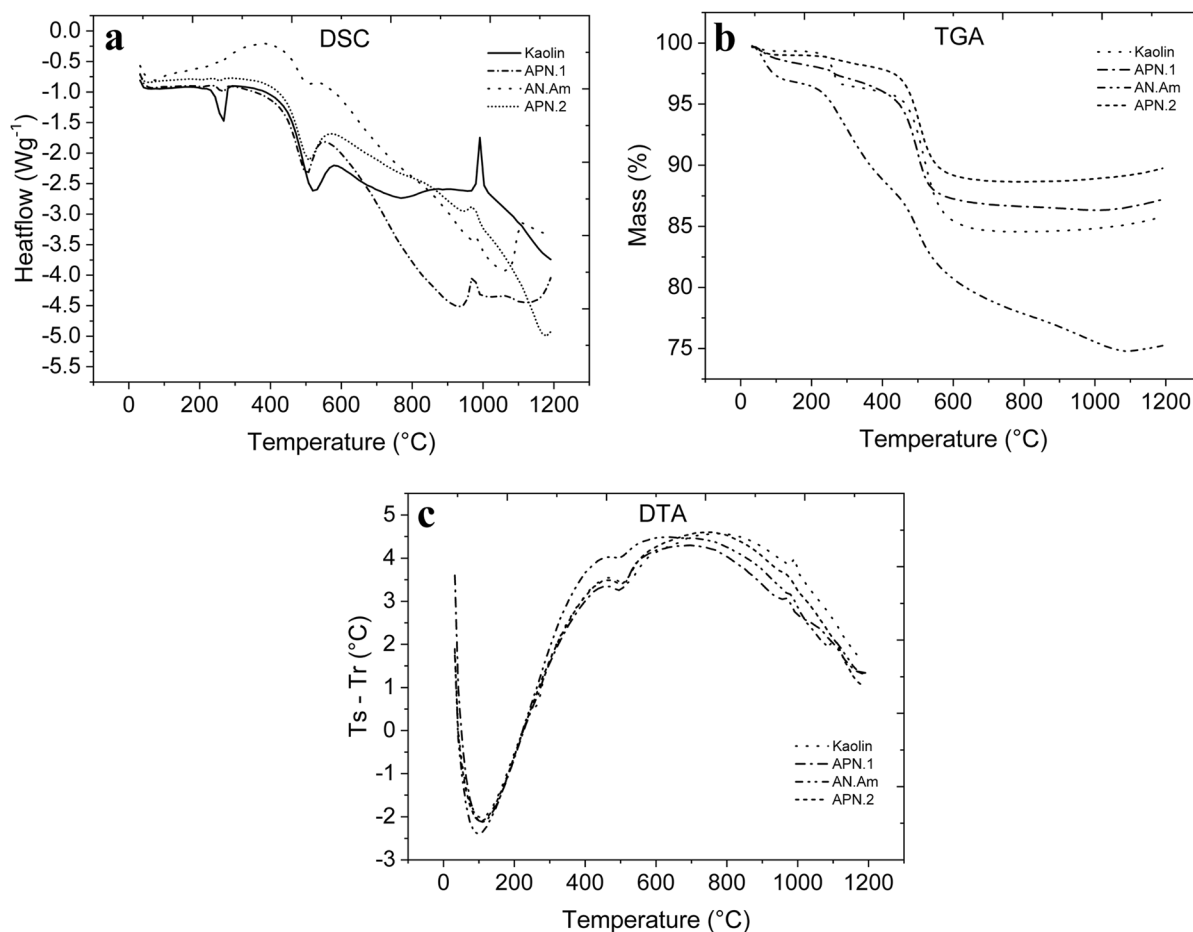The use of kaolin in semi-solid cosmetics and medicinal formulations in the form of peloids has

Fig. 5 **a** DSC, **b** TGA, and **c** DTA curves of the studied clays

been reported in the literature. According to Viseras et al. (2019), this structure allows pharmacological functions, being applied in pelotherapy, wound healing, regenerative medicine, antimicrobial activity, and dermo-cosmetics. Only a few clay minerals with lamellar structures, including kaolin, can be used as excipients in formulations of various solid, liquid, or semi-solid dosages in pharmaceutical and cosmetics products (Kim et al., 2016). Regarding textural findings, despite presenting some mineralogical differences, Amazonian clays can be recommended as raw materials for cosmetics applications.

Particle-Size Distribution

Particle-size analysis of kaolin, APN-1, AN-Am, and APN-2 samples (Fig. 7a) revealed a normal particle-size distribution generally, except for the kaolin sample. Peaks in the particle-size range of 6.4 to 100.2 μm corresponded to a volume ratio of 6.9 to 8.6. Kaolin shows a bimodal curve with a peak grain size of 5.8 μm and a volume ratio of 7.3. This peak indicates a smaller particle size compared to the monomodal samples.

Figure 7b shows the particle size curves based on accumulated volume. These curves were obtained based on the effective diameter (d10). The diameter on the particle-size distribution curve corresponding to 10% finer is defined as the effective size. Effective diameters (d10) were: kaolin 0.61 μm, APN-1 2.27 μm, AN-Am 9.36 μm, and APN-2 10.64 μm.

Between 1.6 and 10.7%, all particles were < 2 μm, except for kaolin. From 11.6% to 42.5%, all particle sizes were between 2 and 20 μm; and from 46.8% to
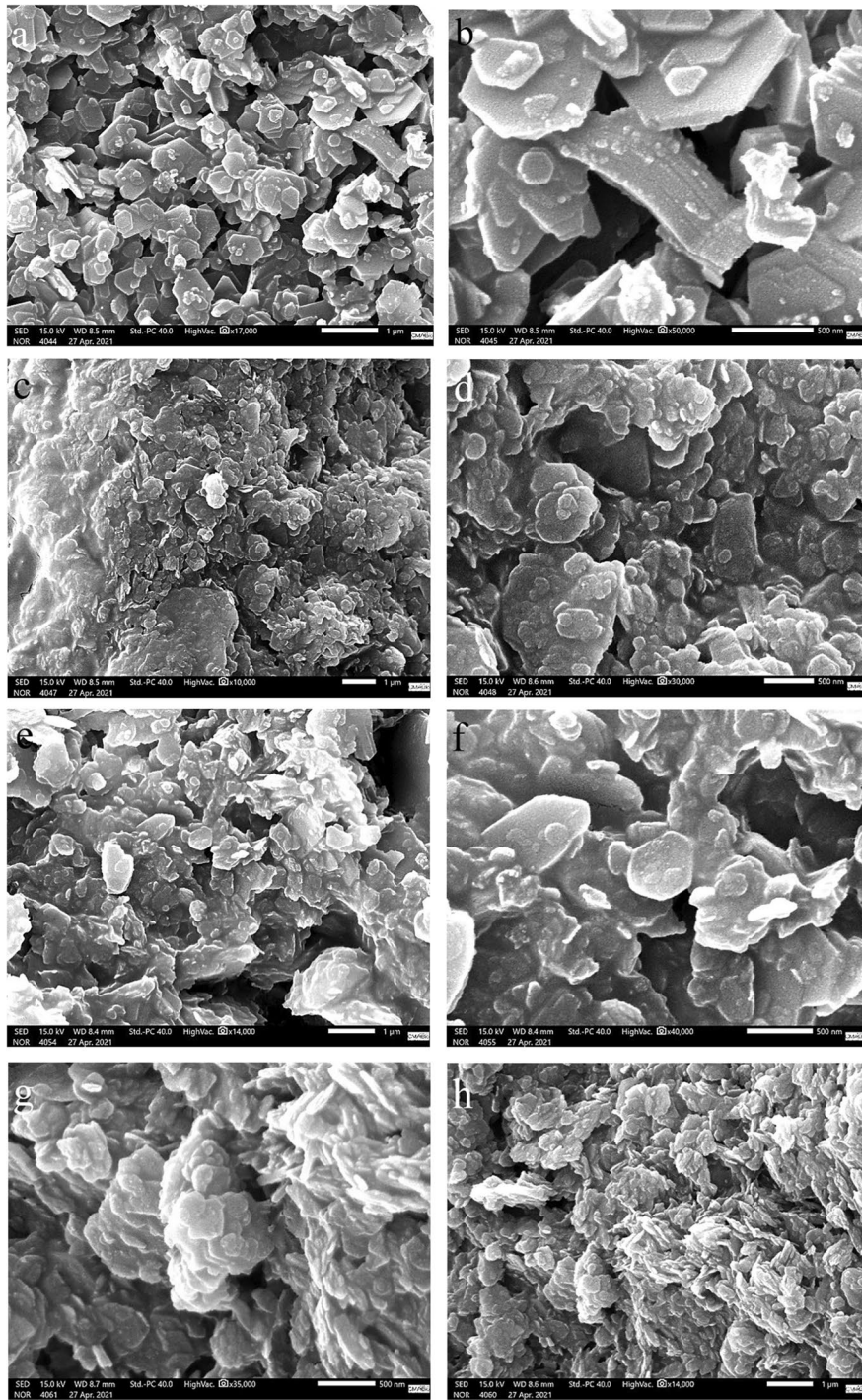
Fig. 6 SEM images of: **a-b** kaolin, **c-d** APN-1, **e-f** AN-Am, and **g-h** APN-2 clays
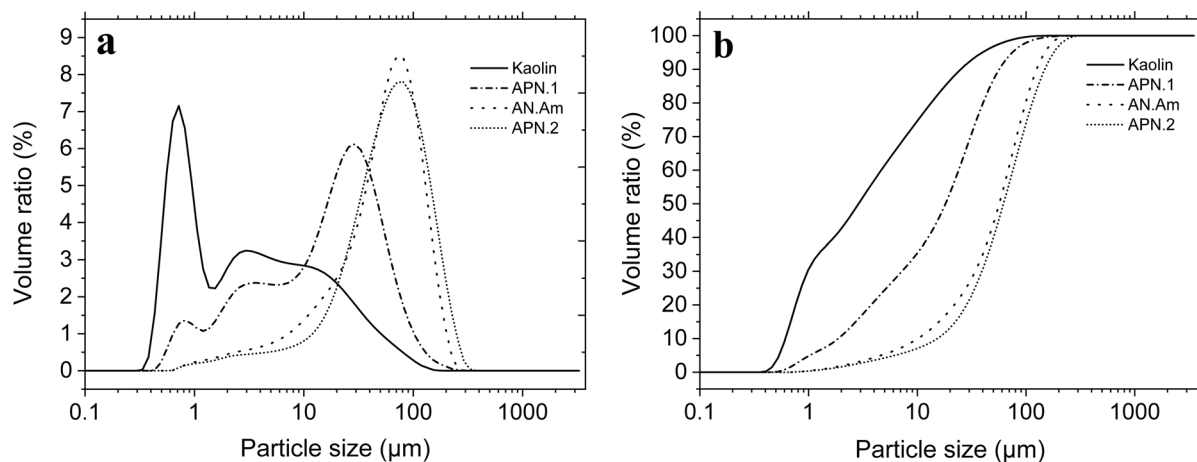
Fig. 7 **a** particle-size distribution, and **b** accumulated volume of kaolinite for APN-1, AN-Am, and APN-2 minerals

86.8%, > 20 μm, which indicated that the minerals other than kaolin have a small 'clay fraction' (particles < 2 μm). The results suggest that kaolin can be used as an emulsifying, pelletizing, granulating, and suspending agent in pharmaceutical formulations (Awad et al., 2017).

Microbiological Analyses

Tests were run for mesophilic bacteria, molds, and yeasts, fecal coliforms, total coliforms, *Escherichia coli*, *Pseudomonas aeruginosa*, and *Staphylococcus aureus*. *Klebsiella* spp is a pathogen, as it is usually involved in several infections, especially in the hospital environment. Its presence is prohibited for products that may be in contact with human skin (Favero et al., 2019). As shown in Table 6, all samples comply with the legislation for use in products for cosmetics applications.

Conclusions

The results indicated that the Amazonian clays offer promise for application in cosmetics materials, such as emulsifying, pelletizing, granulating, and suspending agents. Permissible limits for primary and toxic heavy metals were met for possible application in cosmetics, especially kaolin clay exhibiting a Cr content of < 50 ppm. The dominant phase of the clays belonged to a crystalline triclinic system and the *P*1 space group, known as kaolinite 1A. Other than for the kaolin samples, the existence of a special, commercially rare kaolinite, called kaolinite 2M, was also found, which is part of a dickite-type structure with a monoclinic structure within the *C*1*c*1 space group. A quartz phase, belonging to the $P3_121$ space group, was also noted in the clays. In addition, a gibbsite phase was identified in the APN-1 and kaolin samples. Gibbsite is monoclinic in

Table 6 Results of microbiological tests

Essay	Specification	Kaolin	APN-1	APN-2	AN-Am
Molds and yeasts	-	< 1 CFU/g	< 1 CFU/g	< 1 CFU/g	< 1 CFU/g
Fecal coliforms	Absence in 1 g	Absent	Absent	Absent	Absent
Total coliforms	Absence in 1 g	Absent	Absent	Absent	Absent
Escherichia coli	-	Absent	Absent	Absent	Absent
Klebsiella spp	-	Absent	Absent	Absent	Absent
Mesophilic bacteria	Max. 5000 CFU/g	< 1 CFU/g	< 1 CFU/g	< 1 CFU/g	< 1 CFU/g
Pseudomonas aeruginosa	Absence in 1 g	Absent	Absent	Absent	Absent
Staphylococcus aureus	Absence in 1 g	Absent	Absent	Absent	Absent

the $P12_1/n1$ space group. Based on the crystallographic information file, the clays contained adequate amounts of quartz and iron. The samples revealed a particle-size distribution with a small clay-fraction content, except for the kaolin sample. The samples showed significant plasticity, as demonstrated in the microstructural analysis, mainly for samples APN-1 and APN-2 collected at Manaus. This behavior highlights a possible application in the production of composite materials. Based on microbiological studies, the clays are promising for application in cosmetics products as they meet Brazilian regulations, i.e. Resolution 481/99.

Declarations

Conflict of Interest The authors declare that they have no conflict of interest.

References

ASTM C1365 (2006). Standard Test Method for Determination of the Proportion of Phases in Portland Cement and Portland-Cement Clinker Using X-Ray Powder Diffraction Analysis. ASTM International. West Conshohocken, PA, USA.

ASTM C114 (2013). Standard Test Methods for Chemical Analysis of Hydraulic Cement. ASTM International, West Conshohocken, PA, USA.

ASTM D2216 (2019). Standard Test Methods for Laboratory Determination of Water (Moisture) Content of Soil and Rock by Mass. ASTM International, West Conshohocken, PA, USA.

ASTM D4464 (2015). Standard Test Method for Particle Size Distribution of Catalytic Materials by Laser Light Scattering. ASTM International, West Conshohocken, PA, USA.

ASTM D6913/D6913M (2017). Standard Test Methods for Particle-Size Distribution (Gradation) of Soils Using Sieve Analysis. ASTM International, West Conshohocken, PA, USA.

ASTM E1131 (2020). Standard Test Method for Compositional Analysis by Thermogravimetry. ASTM International, West Conshohocken, PA, USA.

ASTM E1252–98 (2021). Standard Practice for General Techniques for Obtaining Infrared Spectra for Qualitative Analysis. ASTM International, West Conshohocken, PA, USA.

ASTM E1621 (2013). Standard Guide for Elemental Analysis by Wavelength Dispersive X-Ray Fluorescence Spectrometry. ASTM International, West Conshohocken, PA, USA.

ASTM E986 (2004). Standard Practice For Scanning Electron Microscope Beam Size Characterization. ASTM International, West Conshohocken, PA, USA.

Awad, M. E., López-Galindo, A., Setti, M., El-Rahmany, M. M., & Iborra, C. V. (2017). Kaolinite in pharmaceutics and biomedicine. *International Journal of Pharmaceutics, 533*(1), 34–48. https://doi.org/10.1016/j.ijpharm.2017.09.056

Beringhs, A. O., Rosa, J. M., Stulzer, H. K., Budal, R. M., & Sonaglio, D. (2013). Green clay and Aloe Vera peel-off facial masks: Response surface methodology applied to the formulation design. *An Official Journal of the American Association of Pharmaceutical Scientists, 14*, 445–455. https://doi.org/10.1208/s12249-013-9930-8

Bouna, L., Ait El Fakir, A., Benlhachemi, A., Draoui, K., Ezahri, M., Bakiz, B., Villain, S., Guinneton, F., & Elalem, N. (2020). Synthesis and characterization of mesoporous geopolymer based on Moroccan kaolinite rich clay. *Applied Clay Science, 196*, 1–20. https://doi.org/10.1016/j.clay.2020.105764

BRAZIL (1999). Brazilian resolution 481/99: Microbiological control parameters for personal care products and cosmetics. National Health Surveillance Agency ANVISA. Accessed 05/03/2022 https://bvsms.saude.gov.br/bvs/saudelegis/anvisa/1999/res0481_23_09_1999_rep.html

British Pharmacopeia (2008) Accessed 10/12/2021 https://www.pharmacopoeia.com/

Carretero, M. I., & Pozo, M. (2010). Clay and non-clay minerals in the pharmaceutical and cosmetic industries Part II Active Ingredients. *Applied Clay Science, 47*(3–4), 171–181. https://doi.org/10.1016/j.clay.2009.10.016

Chauvel, A., Lucas, Y., & Boulet, R. (1987). On the genesis of the soil mantle of the region of Manaus, Central Amazonia, Brazil. *Experientia, 43*, 234–241. https://doi.org/10.1007/BF01945546

Cornu, S., Lucas, Y., Lebon, E., Ambrosi, J., Luizão, F., Rouiller, J., Bonnay, M., & Neal, C. (1999). Evidence of titanium mobility in soil profiles Manaus, Central Amazonia. *Geoderma, 91*(3–4), 281–295. https://doi.org/10.1016/S0016-7061(99)00007-5

Cosmetic Europe (2019). Cosmetics Europe-the personal care association. Cosmetics and personal care industry overview. Accessed 15/03/2022 https://cosmeticseurope.eu/cosmetics-industry/

Couceiro, P. R. C., & Santana, G. P. (1999). Caulinita em solo da Amazônia: Caracterização e permutabilidade. *Acta Amazônica, 29*(2), 265–275. https://doi.org/10.1590/1809-43921999292275

Das, S., Sen, B., & Debnath, N. (2015). Recent trends in nanomaterials applications in environmental monitoring and remediation. *Environmental Science and Pollution Research, 22*, 18333–18344. https://doi.org/10.1007/s11356-015-5491-6

Favero, J. S., dos Santos, V., Weiss-Angeli, V., Gomes, L. B., Veras, D. G., Dani, N., Mexias, A. S., & Bergmann, C. P. (2019). Evaluation and characterization of Melo Bentonite clay for cosmetic applications. *Applied Clay Science, 175*, 40–46. https://doi.org/10.1016/j.clay.2019.04.004

Ferreira, A. S., Rovani, P. R., de Lima, J. C., & Pereira, A. S. (2015). High-pressure study of Ti50Ni25Fe25 powder produced by mechanical alloying. *Journal of Applied Physics, 117*, 075901. https://doi.org/10.1063/1.4907386

Horbe, A. M. C., Horbe, M. A., & Suguio, K. (2004). Tropical Spodosols in northeastern Amazonas State, Brazil. *Geoderma, 119*, 55–68. https://doi.org/10.1016/S0016-7061(03)00233-7

Ihekweme, G. O., Shondo, J. N., Orisekeh, K. I., Kalu-Uka, G. M., Nwuzor, I. C., & Onwualu, A. P. (2020).

Characterization of certain Nigerian clay minerals for water purification and other industrial applications. *Heliyon, 6*, e03783. https://doi.org/10.1016/j.heliyon.2020.e03783

Kim, M. H., Choi, G., Elzatahry, A., Vinu, A., Choy, Y. B., & Choy, J.-H. (2016). Review of Clay-Drug Hybrid Materials for Biomedical Applications: Administration Routes. *Clays and Clay Minerals, 64*, 115–130. https://doi.org/10.1346/CCMN.2016.0640204

Larson, A. C., & Von Dreele, R. B. G. (2004). General structure analysis system. *Kaos GL Dergisi, 748*, 1–21.

Lebedeva, E. V., & Fogden, A. (2011). Wettability alteration of kaolinite exposed to crude oil in salt solutions. *Colloids and Surfaces A: Physicochemical and Engineering Aspects, 377*, 115–122. https://doi.org/10.1016/j.colsurfa.2010.12.051

Long, M., Zhang, Y., Huang, P., Chang, S., Hu, Y., Yang, Q., Mao, L., & Yang, H. (2018). Emerging Nanoclay Composite for Effective Hemostasis. *Advanced Functional Materials, 28*(10), 1704452. https://doi.org/10.1002/adfm.201704452

López-Galindo, A., Viseras, C., & Cerezo, P. (2007). Compositional, technical and safety specifications of clays to be used as pharmaceutical and cosmetic products. *Applied Clay Science, 36*, 51–63. https://doi.org/10.1016/j.clay.2006.06.016

Ma, G., & Allen, H. C. (2004). *Handbook of Spectroscopy, Volumes 1 and 2* Edited by Günter Gauglitz (University of Tübingen) and Tuan Vo-Dinh (Oak Ridge National Laboratory). Wiley-VCH Verlag GmbH & Co. KGaA: Weinheim. Germany. 1168 pp. *Journal of the American Chemical Society*, 8859–8860 pp. https://doi.org/10.1021/ja033666c

Macedo, R. S., Menezes, R. R., Neves, G. A., & Ferreira, H. C. (2008). Estudo de argilas usadas em cerâmica vermelha (Study of clays used in red ceramic). *Cerâmica, 54*, 411–417. https://doi.org/10.1590/S0366-69132008000400005

Massaro, M., Colletti, C., Lazzara, G., & Riela, S. (2018). The use of some clay.minerals as natural resources for drug carrier applications. *Journal of Functional Biomaterials, 9*, 1–22. https://doi.org/10.3390/jfb9040058

Mattioli, M., Giardini, L., Roselli, C., & Desideri, D. (2016). Mineralogical characterization of commercial clays used in cosmetic and possible risk for health. *Applied Clay Science, 119*(2), 449–454. https://doi.org/10.1016/j.clay.2015.10.023

Melquíades, M. O., de Oliveira, L. S., Rebelo, Q. H. F., Chaudhuri, P., Leite, E. R., Trichês, D. M., & Michielon de Souza, S. (2019). Structural and optical properties of a mechanically alloyed thermoelectric lamellar SnSeS solid solution. *Journal of Applied Physics, 126*, 135707. https://doi.org/10.1063/1.5120033

Michielon de Souza, S., Ordozgoith da Frota, H., Trichês, D. M., Ghosh, A., Chaudhuri, P., dos Santos, S., Gusmao, M., de Figueiredo Pereira, A. F. F., Couto Siqueira, M., Daum Machado, K., & Cardoso de Lima, J. (2016). Pressure-induced polymorphism in nanostructured SnSe. *Journal of Applied Crystallography, 49*, 213–221. https://doi.org/10.1107/S1600576715023663

Morekhure-Mphahlele, R., Focke, W. W., & Grote, W. (2017). Characterization of vumba and ubumba clays used for cosmetic purposes. *South African Journal of Science, 113*, 2–6. https://doi.org/10.17159/sajs.2017/20160105

Muniz, F. T. L., Miranda, M. A. R., Morilla dos Santos, C., & Sasaki, J. M. (2016). The Scherrer equation and the dynamical theory of X-ray diffraction. *Acta Crystallographica*

Section a: Foundations and Advances, 72, 385–390. https://doi.org/10.1107/S205327331600365X

Neto, J. C. M., Kimura, S. P. R., Adeodato, M. G., Neto, J. E., Nascimento, N. R., & Lona, L. M. F. (2017). Intercalation and exfoliation mechanism of kaolinite during the emulsion polymerization. *Chemical Engineering Transactions, 57*, 1453–1458. https://doi.org/10.3303/CET1757243

Otieno, S. O., Kengara, F. O., Kemmegne-Mbouguen, J. C., Langmi, H. W., Kowenje, C. B., & Mokaya, R. (2019). The effects of metakaolinization and fused-metakaolinization on zeolites synthesized from quartz-rich natural clays. *Microporous and Mesoporous Materials, 290*, 109668. https://doi.org/10.1016/j.micromeso.2019.109668

Paiva-Santos, C. O. (2001) Aplicações do método de rietveld e potencialidades do método de scarlett-madse. 1–42. Accessed 13/03/2021 http://noxconsultoria.com.br/labcacc/aulas/textos/Aplicacoes_do_metodo_de_Rietveld.pdf

Reis, N. J., Almeida, M. E., Riker, S. L., & Ferreira A. L. (2006). Geologia e recursos minerais do estado do Amazonas. Rio de janeiro: CPRM; CIAMA, 2006. Accessed 02/03/2022 https://rigeo.cprm.gov.br/handle/doc/2967

Silva, M. S., Lages, A. S., & Santana, G. P. (2017). Physical and chemical study of lattice kaolinites and their interaction with orthophosphate. *Anais Da Academia Brasileira De Ciências, 89*(3), 1391–1401. https://doi.org/10.1590/0001-3765201720160519

Soares de Oliveira, L., de Oliveira Melquiades, M., da Costa Pinto, C., Trichês, D. M., & Michielon de Souza, S. (2020). Phase transformations in a NiTiGe system induced by high energy milling. *Journal of Solid State Chemistry, 281*, 1–8. https://doi.org/10.1016/j.jssc.2019.121056

Souza, W. B., & Santana, G. P. (2014). Mineralogy, zinc kinetic adsorption and sequential extraction of contaminated soil in Manaus Amazon. *Ciencia Rural, 44*(5), 788–793. https://doi.org/10.1590/S0103-84782014000500005

Stokes, A. R., & Wilson, A. J. C. (1944). The diffraction of X-rays by distorted crystal aggregates – I. *Proceedings of the Physical Society, 56*, 174–181. https://doi.org/10.1088/0959-5309/56/3/303

Thiesen, L., Bretzke, P. E., Bittencourt, C. M., Silva, R. M. L., Bresolin, T. M. B., Santin, J. R., & Couto, A. G. (2020). Litchi chinensis leaf extract provides high in vitro photoprotection associated to a natural mineral clay. *Photodermatology, Photoimmunology and Photomedicine, 36*, 61–62. https://doi.org/10.1111/phpp.12488

Toby, B. H. (2006). R factors in Rietveld analysis: How good is good enough? *Powder Diffraction, 21*, 67–70. https://doi.org/10.1154/1.2179804

Vieira Coelho, A. C., Santos, P. D. S., & Santos, H. D. S. (2007). Argilas especiais: O que são, caracterização e propriedades. *Quimica Nova, 30*, 146–152. https://doi.org/10.1590/S0100-40422007000100026

Viseras, C., Carazo, E., Borrego-Sánchez, A., García-Villén, F., Sánchez-Espejo, R., Cerezo, P., & Aguzzi, C. (2019). Clay Minerals in Skin Drug Delivery. *Clays Clay Miner, 67*, 59–71. https://doi.org/10.1007/s42860-018-0003-7

Yadav, T., Mukhopadhyay, N., Tiwari, R., & Srivastava, O. (2005). Studies on the formation and stability of nanocrystalline Al50Cu28Fe22 alloy synthesized through

high-energy ball milling. *Materials Science and Engineering A, 393*, 366–373. https://doi.org/10.1016/j.msea.2004.11.002

Zhao, X., Cai, B., Tang, Q., Tong, Y., & Liu, Y. (2014). One-dimensional nanostructure field-effect sensors for gas detection. *Sensors (switzerland), 14*, 13999–14020. https://doi.org/10.3390/s140813999

Springer